Electronic Supplementary Information for

Key Role of Subsurface Doping in Optimizing Active Sites of IrO_2 for Oxygen Evolution Reaction

Xindi Han, Lei Shi, Hui Chen* and Xiaoxin Zou*

State Key Laboratory of Inorganic Synthesis and Preparative Chemistry, College of Chemistry, Jilin University, Changchun 130012, P. R. China

* E-mail: xxzou@jlu.edu.cn; chenhui@jlu.edu.cn

Methods

1. Computational details

All DFT calculations were employed within the frame of Vienna *ab initio* Simulation Package(VASP 5.4.4).[1,2] The generalized gradient approximation with the Perdew-Burke-Ernzerhof (GGA-PBE) exchange correlation functional was used for the evaluation of exchange-correlation energy.[3] The electron-ion interaction was described using the projector augmented wave (PAW) method[4], and the energy cut-off was set as 450 eV. A 0.05 eV/Å and 10^{-4} eV were adopted for the force and energy threshold criteria, respectively. The Brillouin zones were sampled in the Monkhorst-Pack mesh[5] with k-points separation length of 0.04 2π $Å^{-1}$ for the geometric optimization, and 0.02 2π $Å^{-1}$ for density of states (DOS) calculations, which are created automatically within VASPKIT package[6]. For slab models, half of the upper atoms were fully relaxed while the remaining were kept frozen. A 15 Å vacuum layer was inserted between two slabs to avoid the effect of the interactions from the periodic structure. The dipolar correction was added on the slab models and the symmetrization was taken out of the consideration. The DFT-D3 approach in Grimme's scheme was used to account for the dispersion interaction.[7,8]

2 Calculation Models

2.1 The bulk models of M-IrO_2

To construct M-IrO_2 structure, a 2×2×2 rutile IrO_2 supercell (a = b = 9.01 Å, c = 6.31 Å) was first built and optimized. Then, one M atom was used to substitute one of the 16 Ir atoms in the supercell. The selected doping ratio was 6.25% (1/16). A simplified theoretical model was applied which adopted a metal: O ratio of 1:2 to maintain an ideal rutile structure without any oxygen vacancies, as this study aims to elucidate the impact of the doping metal atom on Ir site in IrO_2. Due to the high symmetry of the IrO_2, there is only one doping configuration (Fig. 1 in main text). After optimization, a series of 59 M-IrO_2 models were obtained.

2.2 The slab models of M_{1-6}-IrO_2

The (110) surface was chosen to study the surface properties, which was the most stable surface for rutile IrO_2.[9] By cleaving from the (110) plane, the surface model of 2×1×4 cell for IrO_2(110) containing four metal layers was constructed. To explore the effect of the doping position, the M atom was doped at six selected sites located at the surface and subsurface of IrO_2(110) model, respectively (denote as M_{1-6}-IrO_2, Fig. 3 in main text, and Fig. S1).

3 Calculation Methods

The formula $MIr_{15}O_{32}$ was used to represent the M-IrO_2 in the following Method Section to give an explicit calculation scheme.

3.1 The forming energy

The forming energy (ΔG_{form}) was evaluated using the approach proposed by Martínez et al.[10] The forming of $MIr_{15}O_{32}$ can be described as following reaction:

$$M + 15Ir + 16O_2 = MIr_{15}O_{32} \quad (1)$$

and ΔG_{form} can be obtained from the following equation:

$$\Delta G_{form} = (E_{MIr15O32} - E_M - 15E_{Ir} - 16G_{O2}) /16 \quad (2)$$

in which $E_{MIr15O32}$, E_M and E_{Ir} were the total energies for $MIr_{15}O_{32}$, M metal per atom and Ir metal per atom. $G(O_2)$ was obtained from the reaction $H_2O \rightarrow H_2 + 1/2O_2$.

3.2 The aqueous stability

The aqueous stability of M atom in $MIr_{15}O_{32}$ were estimated by calculating the corresponding Pourbaix diagram.[11,12] Several possible pathways for M atom transfer from $MIr_{15}O_{32}$ to the aqueous solution are taken in to consideration. The universal chemical equations for these selected pathways are shown as following:

$$MIr_{15}O_{32} + xH_2O \rightarrow (MO_xH_y)^{q+} + ne^- + (2x-y)H^+ + M_{vac}Ir_{15}O_{32} \quad (3)$$

To simulate the acidic OER condition, the pH 0 and the additional bias U from 0 to 1.8V are adopted. At a given U_0, the relative Gibbs free energy can be obtained from the equation below:

$$\Delta G_{(MOxHy)q+}(U_0) = E_{(MOxHy)q+} + E_{MvacIr15O32} + (x-y/2)G_{H2} - xG_{H2O} - E_{MIr15O32} - neU_0 \quad (4)$$

where $E_{MvacIr15O32}$, $E_{MIr15O32}$ are the total energies of $M_{vac}Ir_{15}O_{32}$, $MIr_{15}O_{32}$. G_{H2} and G_{H2O} are the energies of single H_2 and H_2O molecules, respectively. $E_{(MOxHy)q+}$ is obtained from the energy of corresponding M element and $G_{f(MOxHy)q+}$. $G_{f(MOxHy)q+}$ can be found from the database.[11,13,14]

The stability of the remaining structure $M_{vac}Ir_{15}O_{32}$ is also estimated.

$$M_{vac}Ir_{15}O_{32} + 4H^+ + 4e^- \rightarrow 15IrO_2 + 2H_2O \quad (5)$$

$$\Delta G_{vac}(U) = 15E_{IrO2} + 2G_{H2O} - -2G_{H2} - E_{MvacIr15O32} - 4eU \quad (6)$$

$$\Delta G_{vac}(U) = -5.578 - 4eU \quad (7)$$

where for $\Delta G_{vac}(U)$ at U = 0-1.8 V, $\Delta G_{vac}(U)$ is always below 0.

3.3 Theoretical methods for OER

The theoretical catalytic activity of M_{1-6}-IrO_2 for OER was estimated according to the methods developed by Nørskov *et al.*[9] Briefly, the OER process contains four proton-electron coupling elementary steps, as shown in the following:

$$H_2O + * \rightarrow HO^* + H^+ + e^- \quad (8)$$

$$HO^* \rightarrow O^* + H^+ + e^- \quad (9)$$

$$H_2O + O^* \rightarrow HOO^* + H^+ + e^- \quad (10)$$

$$HOO^* \rightarrow O_2 + * + H^+ + e^- \quad (11)$$

in which * is the adsorption site on the surface. In this study, * is coordinately unsaturated Ir site on the surface. HO^*, O^* and HOO^* were three oxygen-containing-intermediates adsorbed on the Ir site.

The Gibbs free energy for each elementary step can be obtained by using a CHE model and the equations are shown as following:

$$\Delta G_1 = E_{HO*} + 1/2E_{H2} - E* - E_{H2O} + (\Delta ZPE - T\Delta S)_1 - eU \quad (12)$$

$$\Delta G_2 = E_{O*} + 1/2E_{H2} - E_{HO*} + (\Delta ZPE - T\Delta S)_2 - eU \quad (13)$$

$$\Delta G_3 = E_{HOO*} + 1/2E_{H2} - E_{O*} - E_{H2O} + (\Delta ZPE - T\Delta S)_3 - eU \quad (14)$$

$$\Delta G_4 = E_* + E_{O2} + 1/2E_{H2} - E_{HOO*} + (\Delta ZPE - T\Delta S)_4 - eU \quad (15)$$

where $E(X)$ (X = *, HO*, O*, HOO*) are the DFT total energies of clean surface and the three intermediates adsorbed on the surface sites, respectively. E_{H2} and E_{H2O} are the energies for single H_2 and H_2O molecule, respectively. The *Gibbs* free energy change for generating an O_2 molecule was fixed according to the experimental value of 4.92 eV, based on the reaction $2H_2O \rightarrow 2H_2+O_2$. The $\Delta ZPE- T\Delta S$ is the zero-point energy and the entropy correction. The correlative values are shown in Table S9. An additional bias was added on each step by considering a $-eU$ term. The potential determined step (PDS) was defined as the most unfavorable thermodynamic step, and the theoretical overpotential can be determined by using $\eta = \max(\Delta G_{1-4})/e - 1.23$ V. Note that we did not consider the Ga_{1-4}-IrO_2, due to the seriously structural reconstruction in the optimized process. The lattice oxygen participating mechanism (LOM), a competing mechanism of the traditional adsorbed evolution mechanism (AEM), is also considered, using the method proposed by Kolpak *et al*.[15]

3.4 The calculation methods for the electronic properties.

a) Work Function

The work function is the energy needed for the electron transferring from the material surface to the vacuum level, and can be used to estimate the ability of the electron transfer in the adsorption process.[16] As shown in Fig. 4d, the theoretical work function (WF) is the energy difference between the vacuum level (E_{vac}) and Fermi level (E_F). E_{vac} can be obtained by assessing the electrostatic potential at a position which is away enough from the surface to prevent the effect of the upper and the lower surface of the slab models.

$$\mathrm{WF} = E_{\mathrm{vac}} - E_F \tag{16}$$

b) e_g-filling for Ir site

The e_g-filling of the surface Ir site was evaluated using the following equation:[17]

$$e_g\text{ - filling } = \int_{-\infty}^{0} \mathrm{n}(\varepsilon)\, \mathrm{d}\varepsilon \tag{17}$$

in which, ε is the energy relative to Fermi level ($E_F = 0$), $\mathrm{n}(\varepsilon)$ is the partial density of states (pDOS) of e_g-orbital of surface Ir site.

c) surface Ir_{5d} and surface O_{2p} band center

The surface Ir_{5d} band center and the surface O_{2p} band center were obtained using following equation:[17]

$$\varepsilon_x = \frac{\int_{-\infty}^{+\infty} n_x(\varepsilon)\varepsilon\, \mathrm{d}\varepsilon}{\int_{-\infty}^{+\infty} n_x(\varepsilon)\, \mathrm{d}\varepsilon} \tag{18}$$

in which, ε is the energy relative to Fermi level ($E_F = 0$), $\mathrm{n_x}(\varepsilon)$ is the partial density of states of the corresponding orbitals (x = Ir_{5d}, O_{2p}).

Table S1. The ΔG_{form} for the 59 possible M-IrO_2 bulk models.

M-IrO_2	ΔG_{form} (eV)	M-IrO_2	ΔG_{form} (eV)	M-IrO_2	ΔG_{form} (eV)	M-IrO_2	ΔG_{form} (eV)
Li	-2.58	Cu	-2.21	In	-2.49	Er	-2.70
Be	-2.17	Zn	-2.56	Sn	-2.43	Tm	-2.41
Na	-2.59	Ga	-2.54	Sb	-1.74	Yb	-2.91
Mg	-2.79	Ge	-1.85	Cs	-2.34	Lu	-3.11
Al	-2.01	Rb	-2.48	Ba	-2.78	Hf	-2.57
K	-2.59	Sr	-2.98	La	-2.75	Ta	-2.68
Ca	-3.00	Y	-2.88	Ce	-2.47	W	-2.51
Sc	-2.77	Zr	-2.40	Pr	-2.58	Re	-2.26
Ti	-2.70	Nb	-2.63	Nd	-2.61	Os	-2.15
V	-2.49	Mo	-2.49	Sm	-2.37	Pt	-1.92
Cr	-2.39	Ru	-2.19	Eu	-2.85	Au	-1.93
Mn	-2.34	Rh	-2.09	Gd	-2.68	Hg	-2.49
Fe	-2.27	Pd	-1.98	Tb	-2.66	Pb	-2.26
Co	-2.20	Ag	-2.15	Dy	-2.68	Bi	-2.27
Ni	-2.16	Cd	-2.50	Ho	-2.69		

Table S2. The species and the corresponding voltage range (U) of 59 M-IrO_2 in Pourbaix diagram.

	Specie-A	U_A(V)	Specie-B	U_B (V)	Specie-C	U_C (V)
Li	Li-IrO_2	0-1.39 V	Li^+	1.39-1.80 V		
Be	Be-IrO_2	0-0.89 V	Be^{2+}	0.89-1.80 V		
Na	Na-IrO_2	0-0.50 V	Na^+	0.50-1.80 V		
Mg	Mg-IrO_2	0-1.29 V	Mg^{2+}	1.29-1.80 V		
Al	Al-IrO_2	0-1.21 V	Al^{3+}	1.21-1.80 V		
K	K-IrO_2	--	K^+	0.00-1.80 V		
Ca	Ca-IrO_2	0-0.46 V	Ca^{2+}	0.46-1.80 V		
Sc	Sc-IrO_2	0-1.16 V	Sc^{3+}	1.16-1.80 V		
Ti	Ti-IrO_2	0-1.37 V	TiO_2	1.37-1.80 V		
V	V-IrO_2	0-1.20 V	V_2O_5	1.20-1.30 V	VO_4^-	1.30-1.80 V
Cr	Cr-IrO_2	0-1.13 V	Cr^{3+}	1.13-1.37 V	$HCrO_4^-$	1.13-1.80 V
Mn	Mn-IrO_2	0-1.32 V	Mn^{2+}	1.32-1.33 V	MnO_2	1.33-1.66 V
					MnO_4^-	1.66-1.80 V
Fe	Fe-IrO_2	0-1.42 V	Fe^{3+}	1.42-1.72 V	FeO_4^-	1.40-1.80 V
Co	Co-IrO_2	0-1.54 V	Co^{2+}	1.54-1.80 V		
Ni	Ni-IrO_2	0-1.21 V	Ni^{2+}	1.21-1.80 V		
Cu	Cu-IrO_2	0-1.53 V	Cu^{2+}	1.53-1.80 V		
Zn	Zn-IrO_2	0-1.38 V	Zn^{2+}	1.38-1.80 V		
Ga	Ga-IrO_2	0-1.35 V	Ga^{3+}	1.35-1.80 V		
Ge	Ge-IrO_2	0-1.16 V	GeO_2	1.16-1.80 V		
Rb	Rb-IrO_2	--	Rb^+	0.00-1.80 V		
Sr	Sr-IrO_2	--	Sr^{2+}	0.00-1.80 V		
Y	Y-IrO_2	0-0.64 V	Y^{3+}	0.64-1.80 V		
Zr	Zr-IrO_2	0-0.95 V	ZrO^{2+}	0.95-1.80 V		
Nb	Nb-IrO_2	0-1.08 V	Nb_2O_5	1.08-1.80 V		
Mo	Mo-IrO_2	0-0.96 V	MoO_3	0.96-1.80 V		
Ru	Ru-IrO_2	0-1.36 V	RuO_4^{2-}	1.36-1.80 V		
Rh	Rh-IrO_2	0-1.50 V	RhO_2	1.50-1.80 V		
Pd	Pd-IrO_2	0-1.51 V	PdO_2	1.51-1.80 V		

Ag	Ag-IrO_2	0-1.12 V	Ag^+	1.12-1.80 V		
Cd	Cd-IrO_2	0-0.96 V	Cd^{2+}	0.96-1.80 V		
In	In-IrO_2	0-1.18 V	In^{3+}	1.18-1.80 V		
Sn	Sn-IrO_2	0-1.27 V	SnO_2	1.27-1.80 V		
Sb	Sb-IrO_2	0-1.27 V	Sb_2O_5	1.27-1.80 V		
Cs	Cs-IrO_2	--	Cs^+	0.00-1.80 V		
Ba	Ba-IrO_2	--	Ba^{2+}	0.00-1.80 V		
La	La-IrO_2	0-0.15 V	La^{3+}	0.15-1.80 V		
Ce	Ce-IrO_2	0-0.56 V	$Ce(OH)^{2+}$	0.56-1.80 V		
Pr	Pr-IrO_2	--	Pr^{3+}	0.00-1.80 V		
Nd	Nd-IrO_2	0-0.06 V	Nd^{3+}	0.06-1.80 V		
Sm	Sm-IrO_2	0-0.26 V	Sm^{3+}	0.26-1.80 V		
Eu	Eu-IrO_2	--	Eu^{3+}	0.00-1.80 V		
Gd	Gd-IrO_2	0-0.58 V	Gd^{3+}	0.58-1.80 V		
Tb	Tb-IrO_2	0-0.68 V	Tb^{3+}	0.68-1.80 V		
Dy	Dy-IrO_2	0-0.59 V	Dy^{3+}	0.59-1.80 V		
Ho	Ho-IrO_2	0-0.73 V	Ho^{3+}	0.73-1.80 V		
Er	Er-IrO_2	0-0.80 V	Er^{3+}	0.80-1.80 V		
Tm	Tm-IrO_2	0-0.88 V	Tm^{3+}	0.88-1.80 V		
Yb	Yb-IrO_2	0-0.37 V	Yb^{3+}	0.37-1.80 V		
Lu	Lu-IrO_2	0-1.01 V	Lu^{3+}	1.01-1.80 V		
Hf	Hf-IrO_2	0-0.94 V	Hf^{4+}	0.94-1.80 V		
Ta	Ta-IrO_2	0-1.10 V	Ta_2O_5	1.10-1.80 V		
W	W-IrO_2	0-0.92 V	WO_3	0.92-1.80 V		
Re	Re-IrO_2	0-1.00 V	ReO_3	1.00-1.38 V	ReO_4^-	1.38-1.80 V
Os	Os-IrO_2	0-1.13 V	OsO_4	1.13-1.80 V		
Pt	Pt-IrO_2	0-1.41 V	PtO_2	1.41-1.80 V		
Au	Au-IrO_2	0-1.23 V	Au_2O_3	1.23-1.80 V		
Hg	Hg-IrO_2	0-0.96 V	Hg_2^{2+}	0.96-1.10 V	Hg^{2+}	1.10-1.80 V
Pb	Pb-IrO_2	0-1.09 V	Pb^{2+}	1.09-1.39 V	PbO_2	1.39-1.80 V
Bi	Bi-IrO_2	0-1.06 V	Bi^{3+}	1.06-1.43 V	BiO_2	1.43-1.80 V

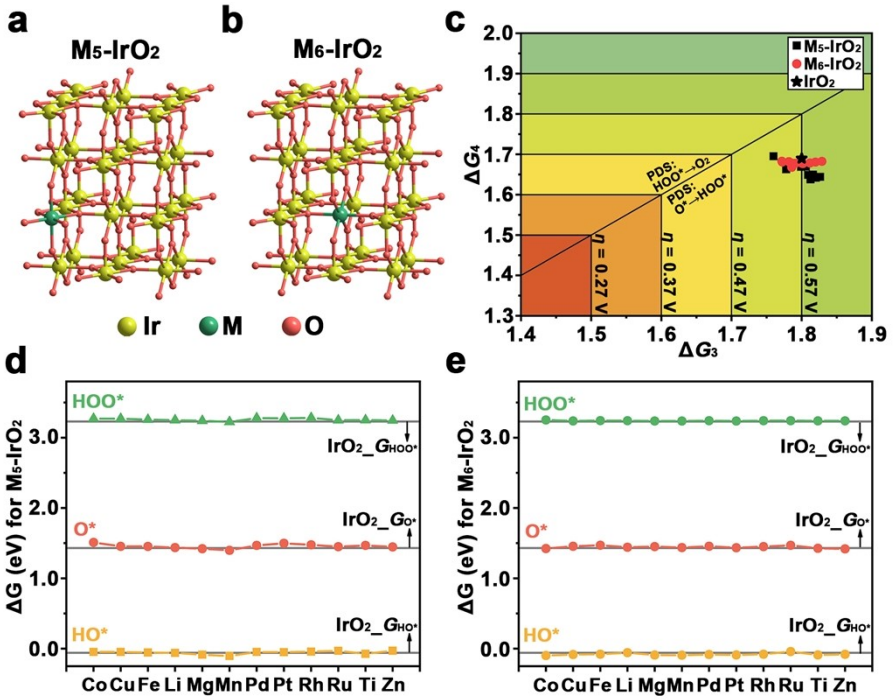

Fig. S1 The schematic of doping positions of a) M_5-IrO_2 and b) M_6-IrO_2, respectively. c) The theoretical overpotentials (η) plot with ΔG_3 and ΔG_4 as descriptors for M_5-IrO_2 and M_6-IrO_2. The ΔG of intermediates as a function of doping metal for d) M_5-IrO_2 and e) M_6-IrO_2.

Besides the $M_{1\text{-}4}$ site, we also explore the adsorption properties and the theoretical overpotential for surface Ir sites in the deeper doping positions, M_5-IrO_2 and M_6-IrO_2 (Fig. S1a,b), respectively. The results in Fig. S1c-e and Table S7,8 show that the adsorption energies of oxygen-containing-intermediates (HO*, O*, HOO*) and theoretical overpotential of the surface Ir sites in M_5-IrO_2 and M_6-IrO_2 are similar to that of IrO_2, which suggests little effects of M_5, M_6 doping sites or deeper on the surface properties.

Table S3. The *Gibbs* free energy for oxygen-intermediates adsorbed on surface Ir site and the OER overpotential (η_{OER}) of M_1-IrO_2, the work function for the M_1-IrO_2 surface, the e_g-filling and the d-band center of the surface Ir site and the O p-band center of the surface oxygen atoms.

M_1 site	ΔG_{HO*} (eV)	ΔG_{O*} (eV)	ΔG_{HOO*} (eV)	η_{OER} (V)	Work Function (eV)	Surface Ir-e_g filling	Ir_{5d} band center (eV)	O_{2p} band center (eV)
Li	-0.01	1.33	3.02	0.67	6.02	2.74	-2.41	-3.05
Mg	-0.03	1.38	3.00	0.69	6.05	2.78	-2.38	-3.18
Ti	-0.04	1.32	2.96	0.73	5.99	2.72	-2.26	-3.18
Mn	-0.07	1.36	2.95	0.74	5.67	2.75	-2.36	-3.37
Fe	-0.05	1.41	2.98	0.71	6.02	2.76	-2.34	-3.18
Co	-0.02	1.47	3.03	0.66	6.23	2.77	-2.42	-3.17
Cu	-0.03	1.32	3.03	0.66	5.88	2.73	-2.42	-3.39
Zn	0.00	1.38	3.02	0.67	6.11	2.77	-2.32	-3.13
Ru	-0.10	1.39	2.98	0.71	5.81	2.74	-2.42	-3.56
Rh	-0.04	1.45	3.03	0.66	6.25	2.74	-2.29	-3.15
Pd	0.00	1.52	3.07	0.62	6.22	2.74	-2.39	-3.29
Pt	0.00	1.50	3.07	0.62	6.20	2.76	-2.33	-3.33

Table S4. The *Gibbs* free energy for oxygen-intermediates adsorbed on surface Ir site and the OER overpotential (η_{OER}) of M_2-IrO_2, the work function for the M_2-IrO_2 surface, the *eg*-filling and the d-band center of the surface Ir site and the O p-band center of the surface oxygen atoms.

M_2 site	ΔG_{HO*} (eV)	ΔG_{O*} (eV)	ΔG_{HOO*} (eV)	η_{OER} (V)	Work Function (eV)	Surface Ir-e_g filling	Ir_{5d} band center (eV)	O_{2p} band center (eV)
Li	0.28	1.68	3.56	0.65	6.53	2.75	-2.63	-3.64
Mg	0.15	1.52	3.41	0.66	6.17	2.77	-2.42	-2.93
Ti	0.01	1.45	3.27	0.59	6.04	2.67	-2.14	-3.22
Mn	0.01	1.42	3.29	0.64	6.13	2.70	-2.12	-3.12
Fe	0.02	1.43	3.29	0.63	6.23	2.74	-2.29	-3.09
Co	0.13	1.56	3.39	0.60	6.41	2.72	-2.29	-3.09
Cu	0.24	1.61	3.49	0.65	6.56	2.77	-2.59	-3.08
Zn	0.19	1.55	3.43	0.65	6.3	2.80	-2.59	-3.02
Ru	-0.06	1.42	3.25	0.60	5.99	2.75	-2.33	-3.36
Rh	-0.02	1.47	3.29	0.59	6.15	2.73	-2.34	-3.18
Pd	0.14	1.63	3.41	0.55	6.45	2.76	-2.44	-3.22
Pt	0.06	1.62	3.34	0.49	6.47	2.81	-2.37	-3.35

Table S5. The *Gibbs* free energy for oxygen-containing-intermediates adsorbed on surface Ir site and the OER overpotential (η_{OER}) of M_3-IrO_2, the work function for the M_3-IrO_2 surface, the e_g-filling and the d-band center of the surface Ir site and the O p-band center of the surface oxygen atoms.

M_3 site	ΔG_{HO*} (eV)	ΔG_{O*} (eV)	ΔG_{HOO*} (eV)	η_{OER} (V)	Work Function (eV)	Surface Ir-e_g filling	Ir_{5d} band center (eV)	O_{2p} band center (eV)
Li	0.32	1.73	3.27	0.42	6.11	2.85	-2.45	-3.39
Mg	0.20	1.67	3.18	0.51	6.06	2.82	-2.46	-3.45
Ti	-0.05	1.53	3.08	0.61	6.08	2.75	-2.35	-3.46
Mn	0.10	1.66	3.12	0.57	6.13	2.80	-2.35	-3.49
Fe	0.09	1.64	3.13	0.56	6.16	2.81	-2.36	-3.39
Co	0.14	1.66	3.18	0.51	6.33	2.80	-2.48	-3.54
Cu	0.30	1.78	3.34	0.35	6.07	2.86	-2.46	-3.44
Zn	0.21	1.68	3.17	0.52	6.07	2.83	-2.51	-3.49
Ru	-0.02	1.52	3.05	0.64	6.09	2.78	-2.51	-3.59
Rh	-0.00	1.51	3.07	0.62	6.08	2.77	-2.35	-3.35
Pd	0.20	1.72	3.17	0.52	6.17	2.86	-2.38	-3.42
Pt	-0.01	1.50	3.10	0.59	6.19	2.78	-2.32	-3.45

Table S6 The *Gibbs* free energy for oxygen-intermediates adsorbed on surface Ir site and the OER overpotential (η_{OER}) of M_4-IrO_2 and rutile IrO_2.

M_4 site	ΔG_{HO*} (eV)	ΔG_{O*} (eV)	ΔG_{HOO*} (eV)	η_{OER} (V)
Li	-0.06	1.45	3.24	0.56
Mg	-0.06	1.44	3.25	0.58
Ti	-0.08	1.46	3.23	0.54
Mn	-0.08	1.45	3.24	0.56
Fe	-0.08	1.43	3.24	0.58
Co	-0.07	1.44	3.24	0.57
Cu	-0.06	1.46	3.24	0.55
Zn	-0.056	1.44	3.25	0.58
Ru	-0.09	1.45	3.25	0.57
Rh	-0.07	1.44	3.25	0.58
Pd	-0.06	1.46	3.24	0.55
Pt	-0.07	1.44	3.24	0.57
IrO_2	-0.06	1.43	3.23	0.56

Table S7 The *Gibbs* free energy for oxygen-intermediates adsorbed on surface Ir site and the OER overpotential (η_{OER}) of M_5-IrO_2.

M_5 site	ΔG_{HO*} (eV)	ΔG_{O*} (eV)	ΔG_{HOO*} (eV)	η_{OER} (V)
Li	-0.04	1.48	3.28	0.57
Mg	-0.03	1.45	3.25	0.57
Ti	-0.05	1.51	3.27	0.53
Mn	-0.05	1.51	3.27	0.53
Fe	-0.05	1.5	3.26	0.53
Co	-0.05	1.47	3.28	0.58
Cu	-0.05	1.45	3.27	0.59
Zn	-0.06	1.45	3.26	0.58
Ru	-0.07	1.47	3.25	0.55
Rh	-0.06	1.44	3.25	0.58
Pd	-0.09	1.42	3.24	0.59
Pt	-0.1	1.4	3.22	0.59

Table S8 The *Gibbs* free energy for oxygen-intermediates adsorbed on surface Ir site and the OER overpotential (η_{OER}) of M_6-IrO_2.

M_6 site	ΔG_{HO*} (eV)	ΔG_{O*} (eV)	ΔG_{HOO*} (eV)	η_{OER} (V)
Li	-0.08	1.45	3.24	0.56
Mg	-0.04	1.47	3.24	0.54
Ti	-0.08	1.42	3.24	0.59
Mn	-0.1	1.42	3.25	0.6
Fe	-0.09	1.44	3.24	0.57
Co	-0.08	1.46	3.24	0.55
Cu	-0.08	1.46	3.24	0.55
Zn	-0.08	1.47	3.24	0.54
Ru	-0.09	1.43	3.24	0.58
Rh	-0.06	1.44	3.24	0.57
Pd	-0.09	1.45	3.24	0.56
Pt	-0.09	1.44	3.24	0.57

Table S9. The Gibbs free energy corrections for gas molecules and adsorbates.

	TS	*ZPE*	E_{DFT}
H_2O	0.67	0.59	-14.24
H_2	0.41	0.30	-6.76
HO^*	0	0.34	
O^*	0	0.07	
HOO^*	0	0.44	

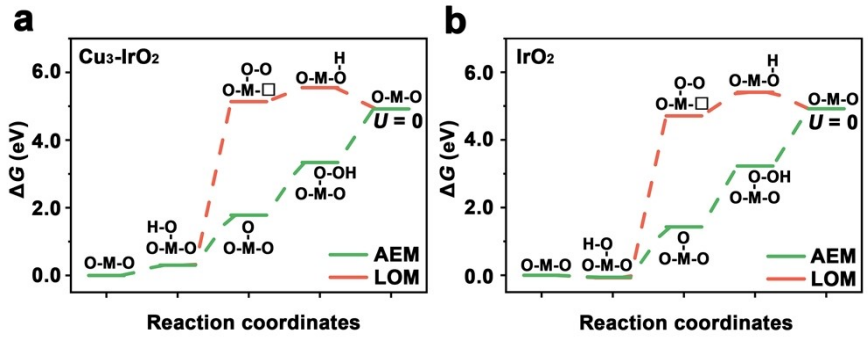

Fig. S2 *Gibbs* free energy diagram of LOM and AEM on a) Cu_3-IrO_2 and b) IrO_2. The inset shows the structure of the reaction intermediates in the two pathways.

We explore the activity of the lattice oxygen in the Cu_3-IrO_2 using the lattice oxygen participating mechanism (LOM) which is a competing pathway of the traditional adsorbed evolution mechanism (AEM). For comparison, the LOM on IrO_2 is also considered. As shown in Fig. S2, LOM pathway shows a much higher energy barrier compared with AEM for both Cu_3-IrO_2 and IrO_2, indicating that for Cu_3-IrO_2 and IrO_2, the OER is more prefer to proceed via AEM pathway. Hence, the lattice oxygen of Cu_3-IrO_2 stays stable during the OER rather than evolving into oxygen molecules.

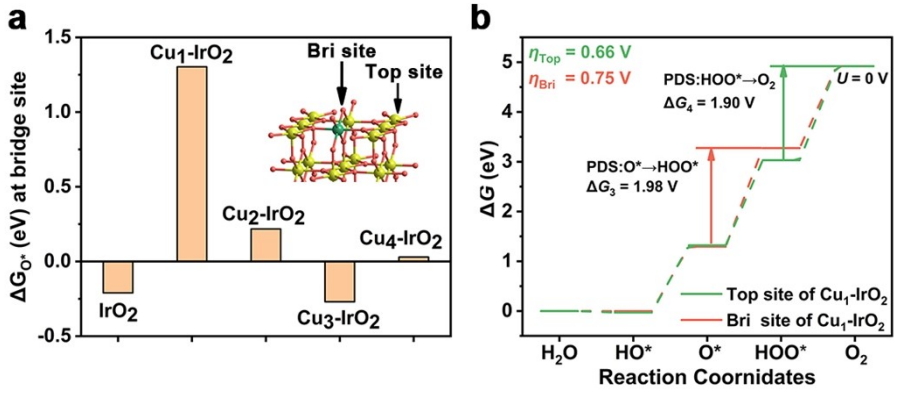

Fig. S3 a) *Gibbs* free energy of oxygen adsorbed on the surface bridge site of IrO_2 and $Cu_{1\text{-}4}IrO_2$, respectively. The inset shows the structural schematic of top site and the bri site. b) *Gibbs* free energy diagram of the top site and the bri site of surface Ir atom of Cu_1-IrO_2.

We explore the adsorption strength of oxygen intermediate on surface bridge site (O_{bri}*) of $Cu_{1\text{-}4}$-IrO_2 and pure IrO_2, respectively. As shown in Fig. S3a**,** the surface Ir bridge sites of $Cu_{2\text{-}4}$-IrO_2 have a strong oxygen adsorption strength, comparable to that of IrO_2, which indicates the poor OER activity of the surface Ir bridge sites of $Cu_{2\text{-}4}$-IrO_2. The Cu_1-doping weakens the oxygen adsorption strength on the surface Ir-Cu bridge site, due to the direct interaction between Cu and O_{bri}*. However, the theoretical overpotential of the surface Ir-Cu bridge site (η = 0.75 V) of Cu_1-IrO_2 is larger than that of the surface Ir top site (η = 0.66 V), as shown in Fig. S3b. The results suggest that after Cu doping, the surface Ir bridge site of $Cu_{1\text{-}4}$-IrO_2 is still inert for OER and the surface Ir top site is the main active site.

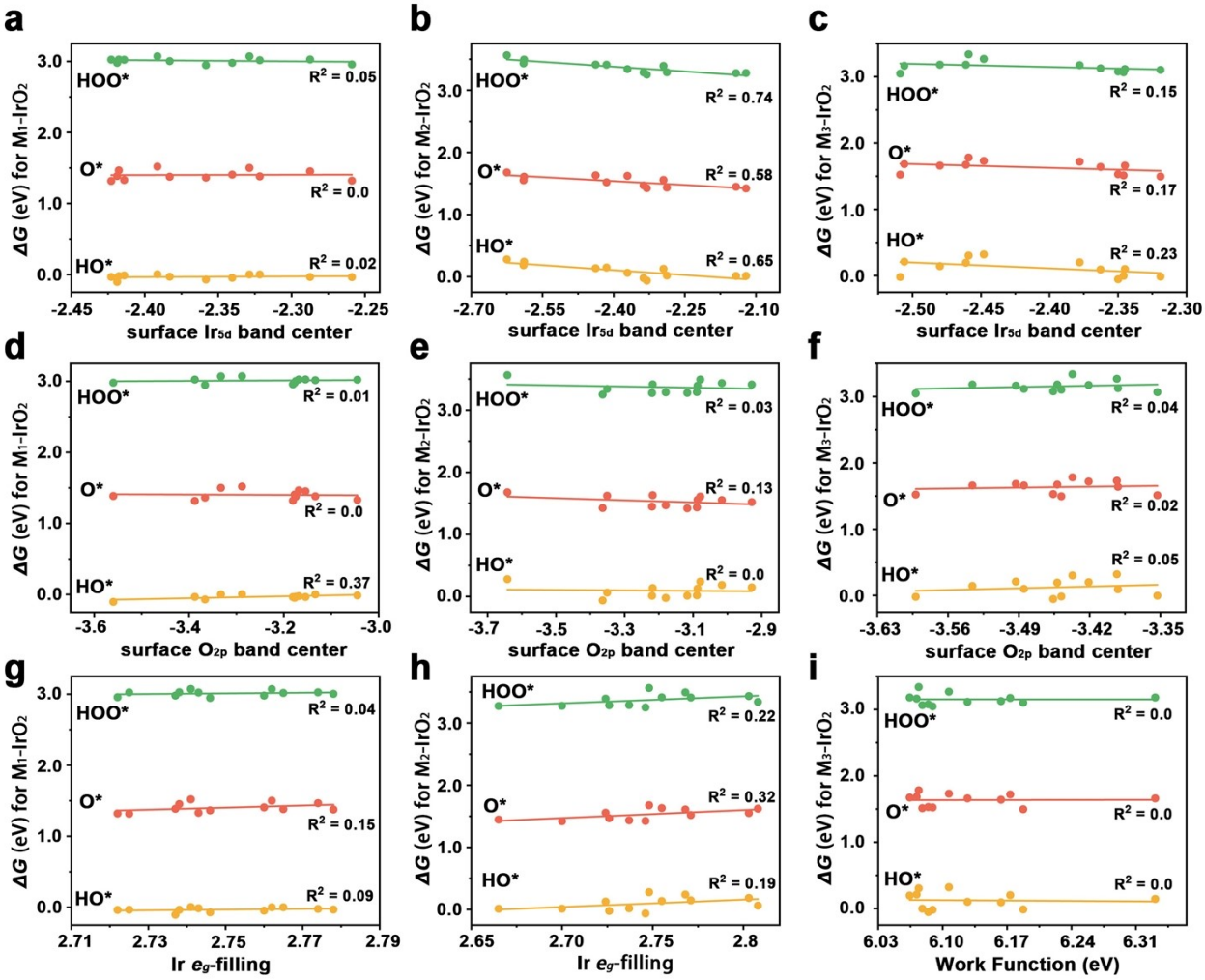

Fig. S4. The ΔG of intermediates as a function of (a-c) Ir_{5d}, (d-f) O_{2p} for $M_{1\text{-}3}IrO_2$, and (g-h) Ir_{eg}.for $M_{1\text{-}2}IrO_2$, (i) WF for M_3IrO_2, respectively.

As shown in Fig. S4, these remaining surface properties exhibit a low linear relationship with the adsorption strength for the intermediates, compared with the linear relationship in Fig. 4a-c in main text. However, we can still find for M_2-IrO_2, the Ir_{5d} changes in the opposite trend with the adsorption energies, which agrees with the d-band center theory.[18] This suggest that the subordinate effect of these properties on the adsorption.

Supplementary References

1. G. Kresse and J. Furthmüller, *Comput. Mater. Sci.*, 1996, **6**, 15.

2. G. Kresse and J. Furthmüller, *Phys. Rev. B*, 1996, **54**, 11169.

3. J. P. Perdew, K. Burke and M. Ernzerhof, *Phys. Rev. Lett*., 1996, **77**, 3865.

4. P. E. Blöchl, *Phys. Rev. B*, 1994, **50**, 17953.

5. H. J. Monkhorst and J. D. Pack, *Phys. Rev. B*, 1976, **13**, 5188.

6. V. Wang, N. Xu, J.-C. Liu, G. Tang and W.-T. Geng, *Comput. Phys. Commun*. 2021, **267**, 108033.

7. S. Grimme, J. Antony, S. Ehrlich and H. Krieg, *J. Chem. Phys*. 2010, **132**, 154104

8. S. Grimme, S. Ehrlich and L. Goerigk, *J. Comput. Chem*. 2011, **32**, 1456

9. J. Rossmeisl, Z.-W. Qu, H. Zhu, G.-J. Kroes and J. K. Nørskov, *J. Electroanal. Chem*. 2007. **607**, 83

10. J. I. Martinez, H. A. Hansen, J. Rossmeisl and J. K. Nørskov, *Phys. Rev. B* 2009, **79,** 045120.

11. M. Pourbaix, Atlas of Electrochemical Equilibria in Aqueous Solutions, *NACE*, 1974.

12. K. A. Persson, B. Waldwick, P. Lazic and G. Ceder, *Phys. Rev. B* 2012, **85**, 235438.

13. J. J. Reed, *J Res Natl Inst Stand Technol*. 2020, Feb 4;**125**:125007.

14. D. D. Wagman, W. H. Evans, V. B. Parker, R. H. Schumm, I. Halow, S. M. Bailey, K. L. Churney and R. L. Nuttall. *J. Phys. Chem. Ref. Data*, 1982, **11**, 1-392.

15. X. Rong, J. Parolin and A. M. Kolpak, *ACS Catal.* 2016, **6**, 1153–1158.

16. L. Lin, R. Jacobs, T. Ma, D. Chen, J. Booske and D. Morgan, *Phys. Rev. Appl.* 2023, **19**, 037001.

17. J. H. Montoya, A. D. Doyle, J. K. Nørskov and A. Vojvodic, *Phys. Chem. Chem. Phys.*, 2018, **20**, 3813.

18. J. K. Nørskov, F. Studt, F. Abild-Pedersen and T. Bligaard, Fundamental Concepts in Heterogeneous Catalysis, *John Wiley & Sons*, Inc., Hoboken, New Jersey, 2014.